Computational Analysis and Flow Physics of a Ducted Rotor in Edgewise Flight

Matthew Misiorowski
Ph.D. Student

Farhan Gandhi
Professor

Assad A. Oberai
Professor

Rensselaer Polytechnic Institute, Troy, NY 12180

ABSTRACT

This study examines the performance of the ducted rotor in hover and edgewise flight conditions. The flow over a three-dimensional model of a ducted rotor was simulated using the Spalart-Allmaras RANS model implemented in a stabilized finite element method. A sliding mesh was used to conveniently account for the large-scale motion associated with rotor revolutions. The simulation results were analyzed to understand the flow physics and quantify the contributions of the rotor and various sections of the duct interior surfaces on the total aerodynamic forces (thrust, drag and side force) and moments (pitching and rolling). In edgewise flight, freestream flow separates off the front of the duct inlet causing a region of recirculating flow and upwash in the rotor plane. The upwash region biases rotor thrust production to the front of the disk. The swirl velocity further biases the region of flow separation over the inlet and upwash at the front of the rotor towards the retreating side of the disk. The shift of thrust production on the rotor and duct towards the front produces a strong nose up pitching moment on the ducted rotor. The rear of the diffuser is a significant contributor to the total drag, this force as incudes a nose down pitch moment which partially negates the moment from the duct inlet. The rotor is the primary source of vertical vibratory forces as well as vibratory pitching and rolling moments. The small tip clearance of the rotor causes a local interaction between the blade tip and duct that is the dominant contributor to in-plane vibratory forces on the ducted rotor.

INTRODUCTION

Ducted rotor designs are attractive to modern rotorcraft designers. Novel designs like the Boeing Phantom Swift, the Urban Aeronautics X-Hawk, and the Aurora Flight Sciences Lightning Strike employ ducted fans to provide some vertical takeoff and landing (VTOL) capability and in some cases as ducted propellers (Refs 1-3). Ducted fans provide an element of safety over open rotors which makes them desirable for manned vehicles and missions operating near people or buildings.

Ducts have been shown to increase the power loading for a rotor by expanding the rotor wake through a diffuser section, reducing the induced power (Ref. 4). Although the expansion of the rotor wake reduces the thrust produced by the rotor, air is drawn by the rotor over the duct inlet, causing a suction similar to the lift generated on the leading edge of an airfoil and provides additional thrust. In a well-designed duct, this additional lift will overcompensate for the reduction in rotor thrust, resulting in a ducted rotor that operates at a higher power loading than the same rotor in isolation.

While ducted rotors have proven aerodynamic advantages in hover, they experience large drag and pitching moments in forward flight. When the edgewise flight velocity dominates the inflow velocity, the front of the duct has a large angle of attack and behaves like an airfoil in deep stall, producing large amounts of lift but with flow separation close to the leading edge of the inlet (Ref. 5). Prior research has been conducted analyzing the performance of ducted fans in axial and edgewise flight as well as specific duct designs attempting to mitigate the deep stall behavior of the upstream section of the duct. This research includes both experimental work and computational analysis.

Pereira and Chopra (Refs. 6, 7) parameterized the duct geometry by inlet curvature, diffuser length and diffuser angle and measured the forces and moments acting on the ducted rotor in axial and edgewise flight. This experiment established trends in ducted rotor performance based on these geometric parameters. The results showed how increasing the radius of curvature of the inlet could delay the separation point on the upstream duct inlet.

Hook, Myers and McLaughlin (Refs. 8, 9) performed experiments on a tandem ducted fan design with two ducted fans arranged longitudinally in the body of an air vehicle. Forces and moments acting on the aircraft were measured and the inlet shape on the front duct was changed attempting to improve vehicle performance. Using flow visualization techniques, this experiment confirmed that altering the inlet design could reduce the separation region on the upstream

Presented at the AHS International 73rd Annual Forum & Technology Display, Fort Worth, Texas, USA, May 9-11, 2017.

duct inlet but it did not significantly affect the aircraft lift or drag.

Martin and Tung performed wind tunnel experiments on an isolated ducted fan in axial and edgewise flight. This experiment recorded the forces and moments acting on the ducted fan while the duct inlet curvature was varied (Ref. 10). The experiment also examined the effect of rotor tip clearance with the duct wall. When the rotor RPM was varied in this study, the angle of attack at which stall occurs on the upstream duct inlet changed significantly, proving that a high induced velocity is required to help keep flow attached to the duct inlet in edgewise flight. Martin and Boxwell further investigated the effect tip clearance has on ducted rotor performance by testing notches in the interior of the duct in the rotor plane. (Ref. 11). Ultimately, the notched duct designs did not significantly change the ducted rotor performance.

Akturk and Camci (Refs. 12, 13, 14) used a combination of experimental and computational methods to analyze ducted fans. Particle image velocimetry (PIV) and wind tunnel experiments were conducted on ducted fans in hover and edgewise flight. These experiments showed that a significant portion of the inflow distribution was affected by the size of the separation bubble on the upstream duct inlet. Further computational analysis was conducted by this group to analyze the effect of rotor tip shapes and a double ducted fan design using computational fluid dynamics (CFD). It was found that decreasing tip clearance improved the performance of the ducted fan and the double ducted fan design is a viable duct inlet separation control device.

The US Army Research Laboratory has conducted computational analysis of ducted fans. Singh and Dinavahi (Ref. 15) coupled CFD analysis with an optimization scheme to design the ideal duct shape. Jimenez and Singh (Ref. 16) used CFD analysis to compare the performance of two different rotor and duct geometry pairs. The first study developed a polynomial surrogate model that was able to predict rotor system performance with 3% of the CFD solution. The second study shows that an untwisted rotor performed more efficiently as a ducted rotor than a rotor with ideal twist. This effect comes from the added downwash on the rotor due to the presence of the duct. Both of these computational studies only looked at axial flow of a ducted rotor in hover.

While prior research has identified the dominant flow phenomena acting on the translating duct (flow separation off the upstream duct inlet), how this separation region interacts with the rotor is not fully understood. The present study uses CFD tools to solve the Reynolds Averaged Navier-Stokes equations (RANS) to provide key insight to the interactional flow features between the rotor and duct and visualize complex flow features at various regions of the ducted rotor. A CFD model of a ducted rotor using a sliding mesh interface to simulate full rotor revolutions was constructed. The study includes variation in performance as a ducted rotor operates in hover and at two different forward flight speeds. Integrated performance metrics such as forces and moments on the ducted rotor and their decomposition will be presented along with a detailed analysis of the flow physics explaining the aerodynamic phenomena and interactions between the rotor and duct. Lastly, this study examines the dominant vibratory forces associated with blade passage frequency and the contribution of the duct to these loads.

METHOD

Coordinate System

This study uses a South, East, Up right-handed coordinate system. The +X is the direction of aircraft drag (or H-force), +Y is out the "right wing" or $\Psi = 90°$ and +Z is in the upward vertical direction.

Ducted Rotor Model

This paper presents the results of a representative ducted rotor configuration. The duct geometry was based on the experiments of Pereira which parameterizes the duct geometry by the inlet radius of curvature, length of the diffuser section, and angle of the diffuser section (Ref. 6, 7). Figure 1 provides a to-scale drawing of the ducted fan describing the duct design parameters, which are given as percentages of the rotor diameter.

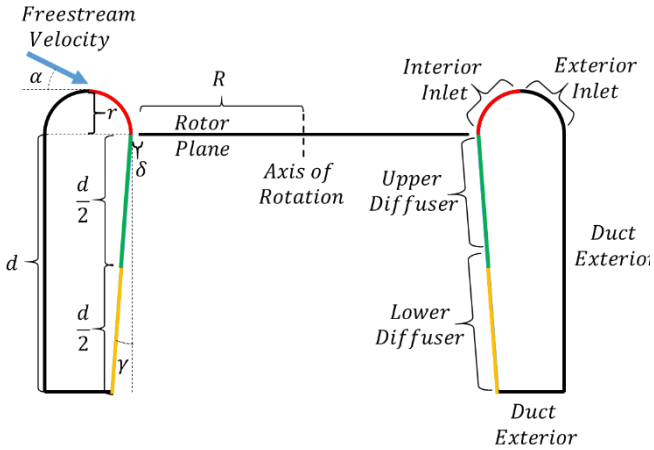

Figure 1: Schematic of ducted rotor system with parameters describing duct geometry

In Figure 1, r represents the radius of the semicircular inlet section, d represents the length of the entire diffuser section, and γ is the diffuser angle. The parameter δ is exaggerated in the figure to become visible and represents the clearance between the rotor tip and duct wall, and R is the rotor radius. The angle α is the relative nose down attitude of the ducted fan relative to the freestream.

Table 1 contains the duct parameters used in this study and are parameterized by the rotor radius.

Table 1: Duct geometry parameters

Parameter	Value
r	26% R
d	144% R
γ	0°
δ	1% R
α	0°
R	15.24 cm (6")

The duct was discretized along the chordwise direction into three surfaces shown in Figure 1: the internal inlet (red), the upper diffuser (green) and the lower diffuser (yellow). This discretization of the duct surfaces facilitates more accurately determining the location of acting forces and moments. While the duct with a semicircular inlet (based on Refs. 6 and 7) was the focus of this study, a deep ducted fan with a lengthy diffuser section is most viable in designs where the fan is embedded in the body of an aircraft such as the Phantom Swift (Ref. 1). Therefore, only integrated thrust and moment values on the duct for the three sections mentioned above are reported. All exterior sections (black) are not reported in this study. In addition to discretizing the duct in the chordwise direction, each of the chordwise surfaces is divided azimuthally in 5 degree increments which provides resolution for determining where around the duct the greatest forces act.

The rotor used in this study is an APC 12x5.5 MR, a commercially available fixed pitch propeller commonly used on small unmanned aerial vehicles (Figure 2).

Figure 2: APC 12x5.5 rotor used in present study

The rotor is hingeless and assumed sufficiently rigid that flapping was not included in the analysis. The actual rotor blade has a rounded tip, however for the purpose of the study a square tip was used.

This rotor is two bladed and the chord and twist along the span of the blade were measured and tabulated in Table 2. The airfoil sections were assumed to be a NACA 4412 at the root, an Eppler 63 at 20% span, and a Clark Y at the tip, using linear interpolation at any point in between.

Table 2: Geometric properties of APC 12 x 5.5 rotor

Radial Position (r)	Local Chord (cm)	Geometric Twist (degrees)
0.1	1.605	20.8
0.2	2.393	32.5
0.3	3.073	27.9
0.4	3.195	21.5
0.5	3.015	18.0
0.6	2.751	14.5
0.7	2.413	11.0
0.8	1.958	9.5
0.9	1.455	8.0
1	1.130	6.5

A tip clearance (measured from the half chord of the rotor tip to the duct wall) of 0.1524 cm or 1% or the rotor radius was used in the model. The rotor is assumed to have zero sweep along the line connecting the 50% chord point of each airfoil section. The circular rotor hub is included in the CFD simulation and has a radius of 0.826 cm, resulting in a 5.4% root cutout.

The ducted rotor was simulated in hover conditions as well as translational flight conditions of 5 and 10 m/s. The rotor speed was maintained at 4300 RPM regardless of flight condition and the ducted fan remained at 0° nose down attitude. This ducted fan was not trimmed to any flight condition but the resulting lift, drag, pitching moment, etc. are calculated and reported.

Computational Method

A computational analysis was conducted about the ducted rotor in hover and two forward flight speeds. A three-dimensional transient solution to the RANS equations was determined using AcuSolve, a stabilized 2nd order upwind finite element solver specifically designed for incompressible or weakly compressible flows up to local Mach numbers of 0.8 (Ref. 17). The advancing rotor blade in this study saw freestream Mach numbers less than 0.23 when the ducted fan translated at 10 m/s, therefore an incompressible solver was suitable. For modeling turbulence the Spalart-Allmaras RANS model was used. The Reynolds number for the duct, based on a typical axial speed of 10 m/s (average velocity induced by the rotor) and the height = $d + r = 0.26$ m, was approximately $1.66 \cdot 10^5$. The Reynolds number for the blades based on the chord and the tangential speed at $0.75R$ for 4,300 RPM was approximately $9.19 \cdot 10^4$. The flow at these Reynolds numbers is expected to be transitional for moderate angles of attack. However, given the effective angles of attack are rather large so that significant separation is anticipated and the incoming flow is likely to be unsteady, a turbulent approximation is a reasonable choice.

The computational domain is shown in Figure 3, an inflow with prescribed velocity and an outflow with zero pressure offset boundary were defined. Other boundaries of the control volume were set to far field which allowed flow to cross the

boundary in either direction with no pressure offset. In the hover case, the inlet and outlet were also set to far field.

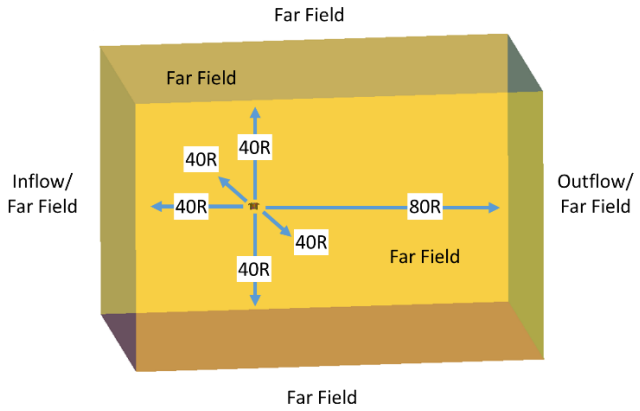

Figure 3: Computational domain and boundary conditions for computational model

A sliding mesh interface was employed to simulate full rotor revolutions in this study. The sliding mesh method requires two separate volumes inside the computational domain: one volume that rotates with respect to the inertial frame and one that remains stationary. These two volumes are coincident only along the sliding interface surface which passes information between the two volumes. Figure 4 shows the rotating volume and sliding interface along with the non-rotating volume. The rotating volume is a cylinder centered about the rotor hub; it has a radius of 15.316 cm and extends both above and below the rotor plane by 2.54 cm. The radius of this rotating volume is such that it ends in the middle of the tip gap clearance. The rotor radius is 0.1524 cm, this results in 0.0762 cm inside the rotating volume between the rotor tip and the sliding interface and 0.0762 cm between the sliding interface and duct wall in the non-rotating volume.

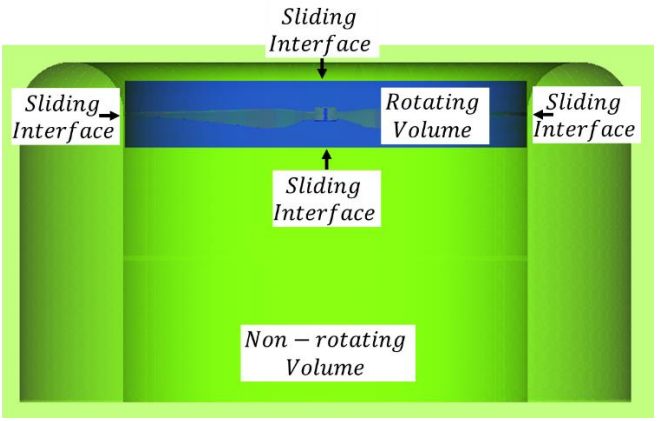

Figure 4: Sliding interface between the non-rotating volume containing the duct and the rotating volume containing the rotor

The domain was discretized using a meshing software developed by Simmetrix (Ref. 18). The mesh was a combination of structured and unstructured tetrahedral finite elements. A structured mesh was generated on the upper and lower surface of the rotor blade. This is accomplished by first discretizing the curve defined by the airfoil cross-section at a given radial location, and then extruding this in the spanwise direction. Controlling the mesh parameters along the curve offers control in resolution along the chord of the blade (50 elements on each the upper and lower surface) while also refining the element size near the leading edge. The elements near the leading edge (0-10% chord) were ten times smaller than the elements along the remaining 90% of the chord. These smaller elements allowed improved resolution of the stagnation point at the leading edge of the airfoil where velocity gradients are high in the chordwise direction. Since velocity gradients in the spanwise direction were lower, anisotropic elements were used. The elements were 0.0762 cm in the spanwise direction, or an aspect ratio of 3:1 compared to the chordwise element size.

The surface of the duct was also discretized using a structured mesh. The mesh was uniform in the circumferential direction with 3,600 divisions. In the vertical direction, which corresponds to the chord of the duct, 50 divisions were used. They were concentrated at the inlet region, where the size was reduced by a factor of 10. They were also concentrated within $\pm 0.1R$ of the rotor plane, where the element size is locally reduced to 0.0254 cm; this is the same size as the elements on the rotor tip as shown in Figure 5.

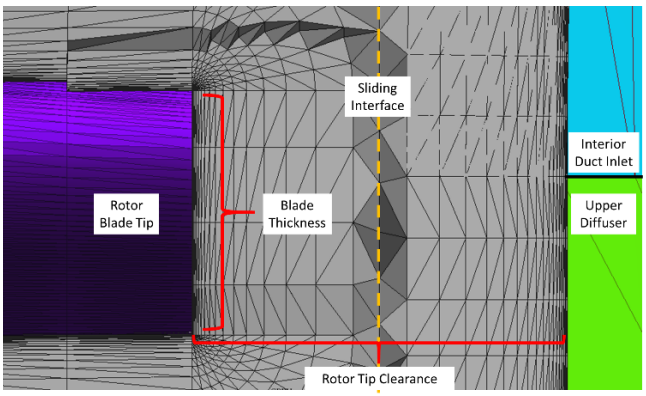

Figure 5: Cut plane of ducted rotor mesh in the region between the rotor tip and duct wall from looking down the chord of the blade

On both the rotor and the duct a structured boundary layer mesh was employed. The first element height was set to ensure y+$\lesssim$ 1 throughout. The y+ was estimated as air over a flat plate with the velocity corresponding to the tip speed of the rotor (68 m/s). The mesh consisted of 52 million elements in total with 5 million coming from the rotating volume and 47 million coming from the non-rotating volume.

A mesh refinement study was conducted by varying the following parameters: size of elements along the chord of the rotor, the leading reduction ratio, the aspect ratio of elements

along the span of the rotor, the chordwise elements on the duct, the local element size near the rotor plane, the azimuthal element size on the duct, and the number of elements in the boundary layer. Each parameter was independently double in refinement, convergence was determined when the thrust and torque changed by less than 1% from the previous setting. The values specified in this section are the results of this convergence study.

The rotor was simulated spinning at 4300 RPM for all flight conditions. All cases were run for 60 revolutions at 10° timesteps, then each simulation was restarted for an additional 2 revolutions at 1° timesteps. While the residuals converged to satisfactory levels within the first 10 revolutions (approximately the time required for fluid particles to completely traverse the length of the duct) a large number of simulated revolutions was required for the ducted rotor in forward flight for long period transient behavior associated with rotor startup to completely dampen out and for the force and moment values to converge.

Most runs were performed on 128 2.6 GHz Intel Xeon E5-2650 processors part of the Center for Computational Innovations (CCI) at Rensselaer Polytechnic Institute. Meshing was completed using the higher memory 3.3 GHz Intel Xeon E5-2643 processor with 256 GB of system memory, also part of the CCI facility.

VARIATION IN FLIGHT SPEED

For the ducted rotor both hover and forward flight (at 5 m/s and 10 m/s) are considered. As the ducted fan in this study has zero nose down attitude, the duct inlet behaves like an airfoil where the angle of attack is determined by the relative freestream velocity and induced velocity of the rotor, as shown in Figure 6.

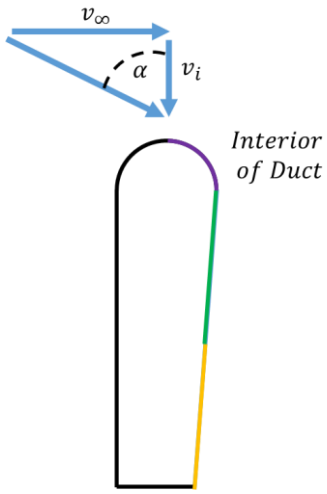

Figure 6: Effective angle of attack on duct inlet due to freestream velocity and induced inflow

Since the freestream velocity (v_∞) is much larger than the induced velocity (v_i) even at moderate flight speeds, the effective angle of attack of the duct inlet is nearly 90° which places the forward section of the duct inlet in deep stall. Flow separates off the duct inlet resulting in an area of low pressure and vorticity in the region of separation (seen in Figure 7).

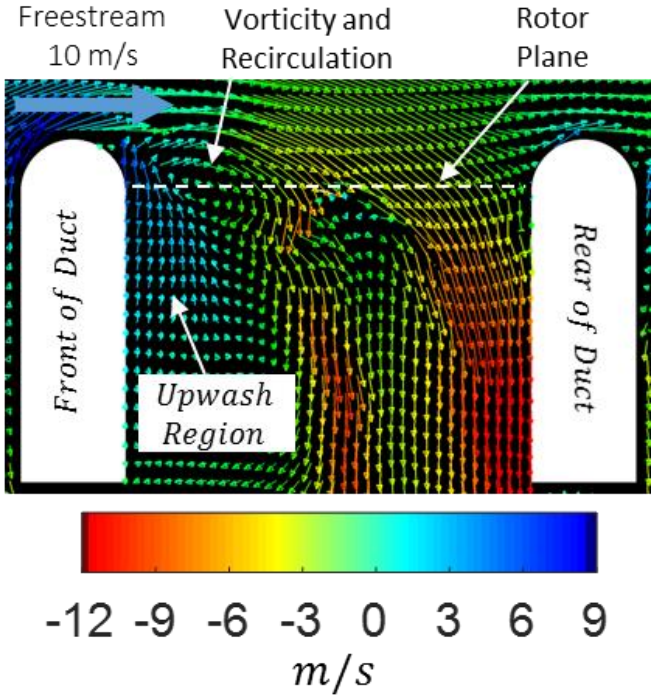

Figure 7: Velocity vectors of flow inside duct colored by axial velocity

This separation extends azimuthally around the forward section of the duct inlet and affects the behavior of the duct and the rotor both in the steady forces and moments on the aerodynamic bodies as well as the vibratory loads. The following sections will detail the interaction between the rotor and separation region on the duct inlet and how the performance characteristics of the ducted fan change with flight speed.

Rotor Aerodynamics

Analysis of the ducted fan shows that the rotor experiences a unique flow phenomenon in forward flight due to the presence of the duct. The flow physics that affect the rotor performance will be investigated in this section.

Figure 8 shows that in edgewise flight the peak rotor thrust is generated at the front of the disk. This is unlike a fixed pitch open rotor where the highest lift is expected on the advancing side due to increased dynamic pressure. As flight speed increases the total thrust production of the rotor increases and is shifted further towards the front of the disk.

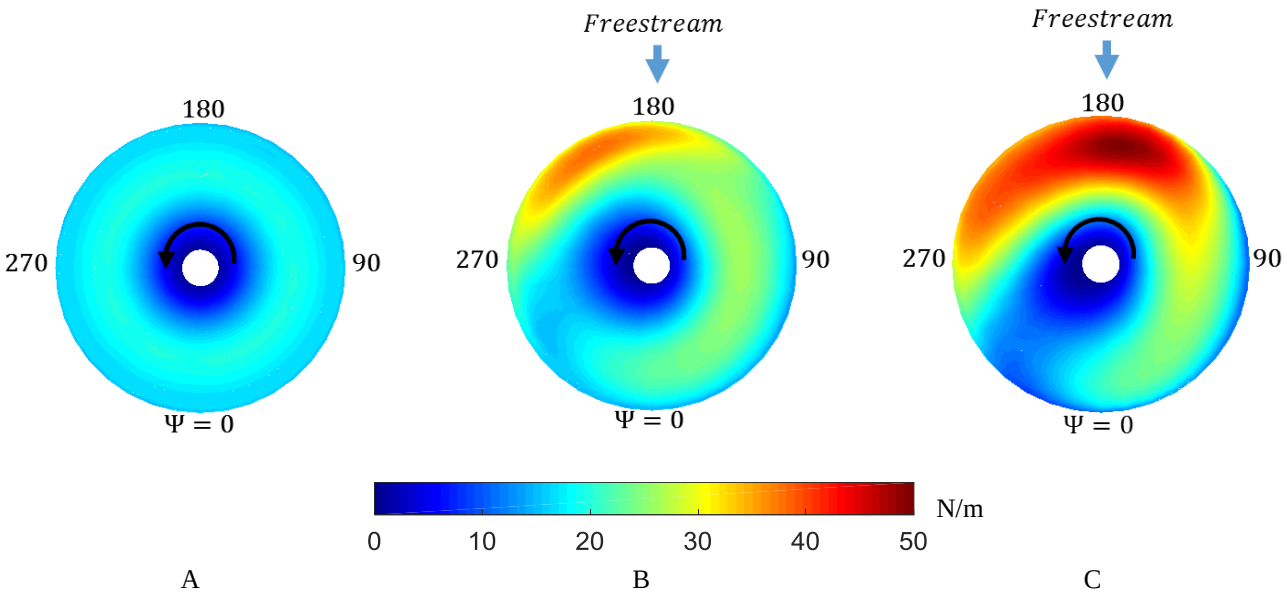

Figure 8: Blade elemental thrust of the ducted rotor in (A) hover, (B) 5 m/s, and (C) 10 m/s forward flight conditions

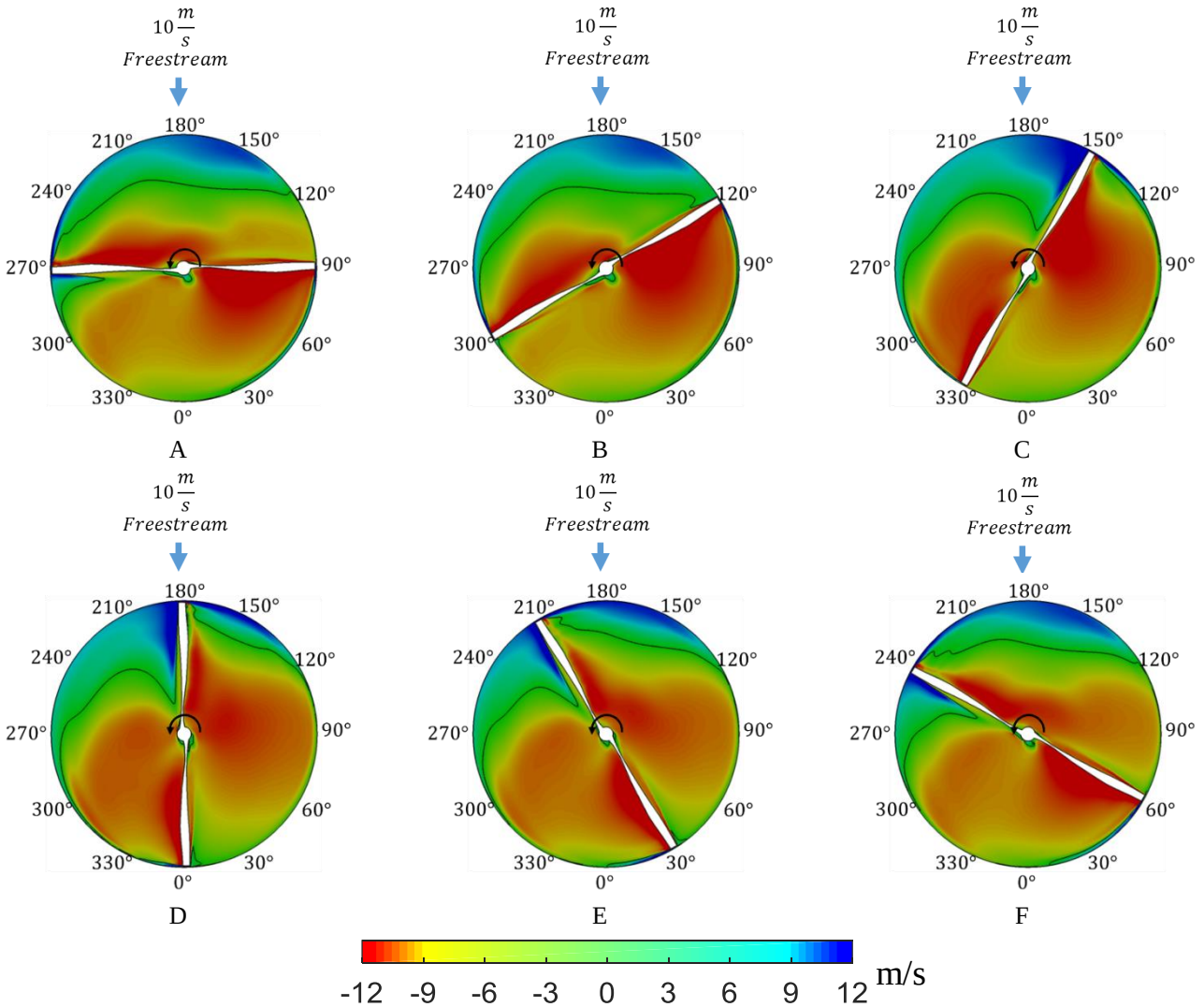

Figure 9: Axial velocity through the rotor plane of the ducted fan translating at 10 m/s as the rotor passes through separation region

The flow separation region on the duct inlet results in an area of recirculation near the rotor plane (Figure 7). This induces an upwash through the rotor plane in the front portion of the disk. This cut plane is along the $\Psi = 0° - 180°$ line while the blades are currently at 90° and 270°. When the blade rotates through this region it will see an upwash on the outboard parts of the blade. The upwash increases the effective angle of attack locally and ultimately produces more lift in this region. This is confirmed by the distribution shown in the disk plots of rotor thrust (Figure 8).

In the disk plot of rotor thrust (Figure 8) there is also lateral distribution, the thrust near the front of the disk is biased to the retreating side. As the blade enters the upwash region near $\Psi = 120°$ (Figure 9), the blade interacts with the slow moving upwash and pushes it along with the blade in the direction of rotation. The black line represents the line of zero axial velocity. All area on the red side of this line corresponds to flow traveling down through the rotor and into the diffuser section of the duct, all area on the blue side of this line corresponds to upwash through the rotor plane. As the blade cuts through this region the upwash stacks up along the span of the blade moving more lift inboard. Figure 9 D shows the blades at $\Psi = 0°$ and $\Psi = 180°$. At this point approximately the outboard 70% of the blade at the front of the disk sees relative upwash. This upwash increases the lift of the blades at these spanwise locations and agrees with the blade elemental thrust distribution (Figure 8) at $\Psi = 180°$.

The disk plots of blade elemental drag in Figure 10 show the variation with increasing forward flight speed. These plots show that the drag on the rotor is highest near the midspan on the advancing side. This spanwise location has the highest geometric twist and largest chord which causes the high drag. This is also the azimuthal location that sees the highest dynamic pressure due to the freestream velocity. Although the front of the disk sees the highest lift, the upwash in that region reduces the induced drag on the blade, which in turn limits the total rotor drag.

The overall steady forces and moments on the rotor are averaged over a revolution and will be reported in a subsequent section focused on the overall performance metrics of the ducted fan as a function of translational speed.

Duct Aerodynamics

The duct significantly contributes to the full vehicle integrated forces and moments. The primary forces acting on the duct are the thrust and drag (H-force), and the primary moment on the duct is nose up pitching. All moments presented in this study are taken about the rotor hub. The pitching moment arises from azimuthal asymmetry of the thrust and H-force around the duct on the inlet and diffuser sections. The duct forces and moments presented in this section are the steady loads on the duct and are time averaged over one revolution.

Figure 11 shows the azimuthal distribution of the duct thrust (defined as total force acting vertically in the +Z direction), in hover and at 5 m/s and 10 m/s forward speed. Moving to forward flight the thrust production on the duct is seen to increase and move to the front. In hover as well as in forward flight, the majority of the thrust is produced by the inlet with no significant contribution from the diffuser section. Even with the front half of the duct behaving like an airfoil in deep stall and the flow separating off the inlet, the duct inlet produces a significant amount of lift.

A secondary effect is the rotor swirl biasing the upwash and duct inlet separation region slightly to the retreating side of the inlet. Figure 12 shows pressure on the front inlet. The separation region having moved slightly to the retreating side is evident in the lower magnitude of suction pressures than seen on the advancing side. The suction pressure magnitudes from $\Psi = 120° - 150°$ are much higher than those from $210° - 240°$). This is consistent with the higher duct thrust seen at $\Psi = 135°$ compared to $\Psi = 225°$ on Figure 11 B and C.

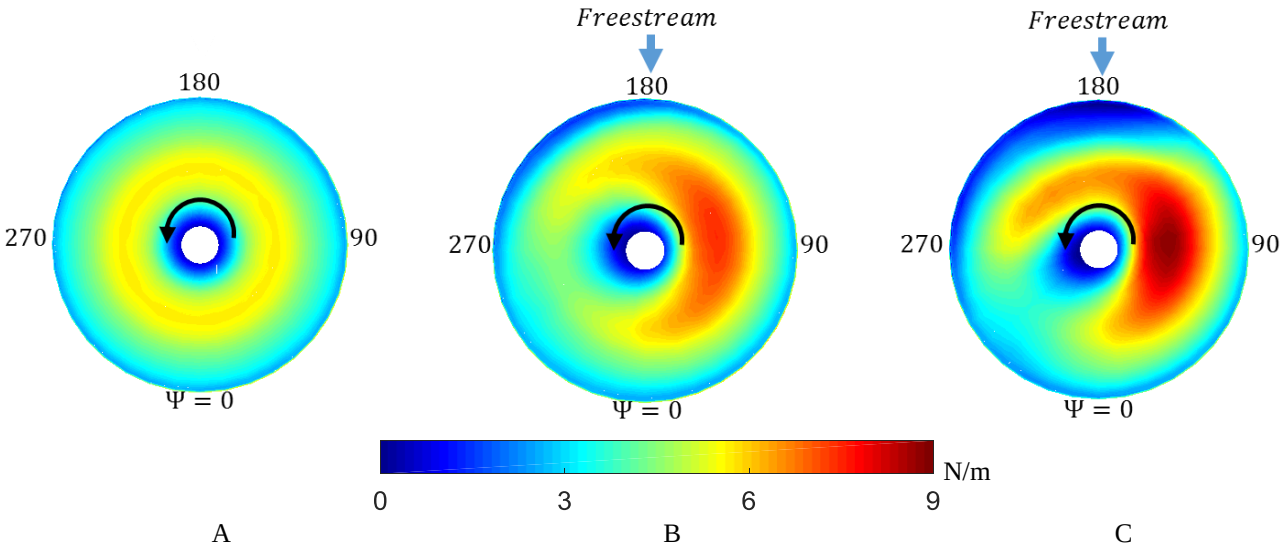

Figure 10: Blade elemental drag of the ducted rotor in (A) hover, (B) 5 m/s, and (C) 10 m/s forward flight conditions

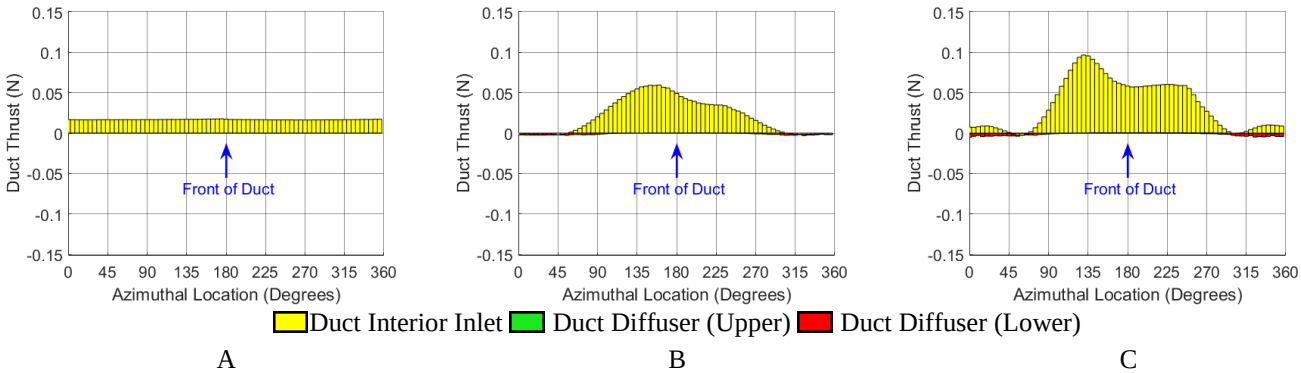

Figure 11: Azimuthal breakup of duct thrust in (A) hover, (B) 5 m/s, and (C) 10 m/s forward flight conditions time averaged over one rotor revolution

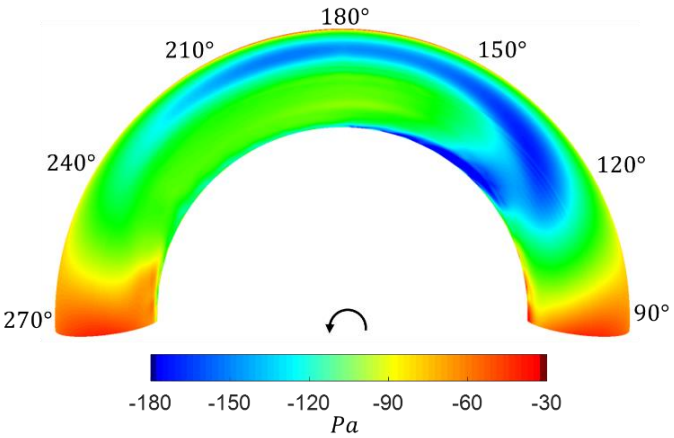

Figure 12: Lateral pressure variation on duct inlet at 10 m/s forward flight speed (time averaged over one revolution)

Figure 13 shows the time averaged axial velocity over the course of one revolution, the cut plane is taken 0.13R above the rotor plane as this height corresponds to half the height of the duct inlet. The black line represents zero axial velocity. The red area indicates induced inflow being drawn into the rotor, while the blue region represents upwash. The upwash seen on Figure 13 between $\Psi = 135°$ and $\Psi = 260°$ is indicative of flow separation on the front inlet.

Figure 14 shows the azimuthal distribution of H-force on the duct. In hover, the induced velocity by the rotor draws in air over the duct inlet and the flow remains attached as it exits the diffuser sections. The normal force created by this attached flow has a radially inward component toward the center of the duct. As expected in hover, these forces cancel and there is no net H-force on the duct. In forward flight conditions the drag comes primarily from two sources, the suction on the front of the duct and the ram pressure from the stagnation of the freestream on the rear of the duct (primarily on the diffuser).

The upwash region at the front of the duct extends vertically into the diffuser sections. This region sees a reduction in pressure causing a small suction on the diffuser sections which adds to the total H-force.

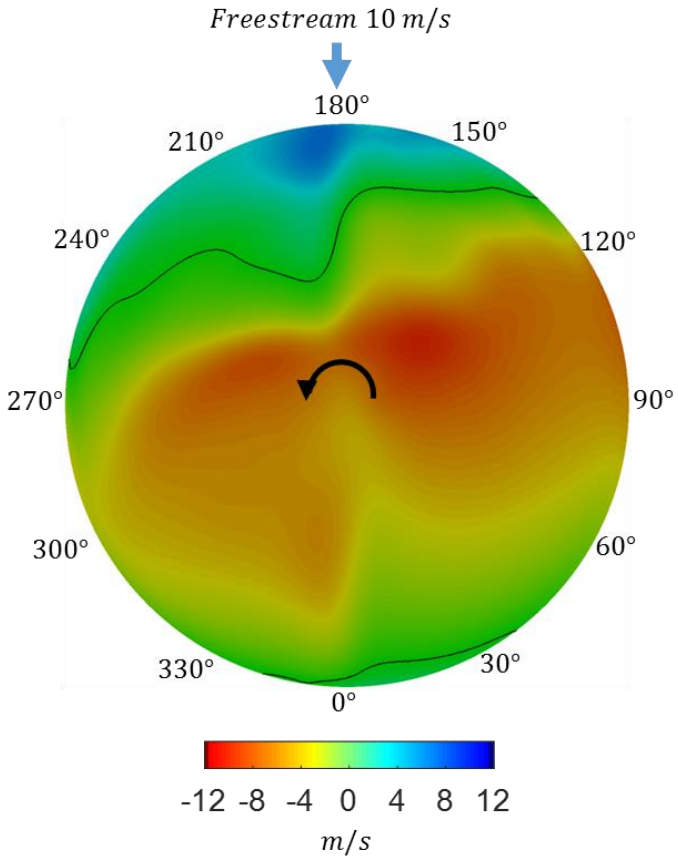

Figure 13: Axial velocity in plane 0.13R above rotor time averaged over one revolution, negative velocity is through the rotor plane and positive velocity is upwash

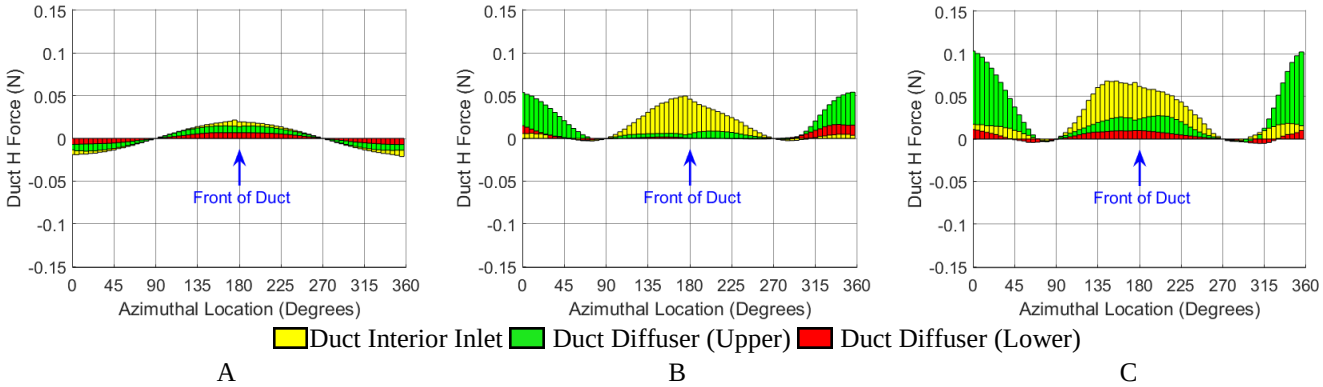

Figure 14: Azimuthal breakup of duct H-force in (A) hover, (B) 5 m/s, and (C) 10 m/s forward flight conditions time averaged over one rotor revolution

The first source of drag on the duct comes from the radial component of suction on the inlet. At the front of the duct this component acts in the direction of aircraft drag.

The ram pressure at the rear of the duct is seen in Figure 15, corresponding to 10 m/s forward flight speed. The rotor induces an inflow which attempts to turn the flow 90° from its freestream velocity to one aligned with the Z (vertical) axis of the duct. However, when the induced inflow velocity is much lower than the freestream velocity the rotor only manages to turn the air slightly downward. This flow collides with the rear of the duct near the rotor plane. The location of this stagnation area vertically on the duct will depend on the magnitude of the rotor induced velocity relative to the freestream velocity.

Finally, Figure 16 shows the azimuthal variation in pitching moment around the duct at the analyzed flight conditions. The pitching moment comes predominantly from the duct thrust at the front inlet. The H-force on the duct is a secondary contributor.

The duct H-force (Figure 14) also affects the total pitching moment taken about the rotor hub. While the H-force on the duct was always positive (+X direction) on the inlet and diffuser sections, the azimuthal location and height relative to the rotor plane dictate the direction of the induced pitching moment. The positive H-force on the interior inlet near $\Psi = 180°$ and $\Psi = 0°$ induces a nose up moment about the rotor hub. The H-force on the upper diffuser section at these same azimuthal locations, being below the rotor plane, induces a nose down moment. While the H-force is in places stronger than the duct thrust, the small moment arm between the drag sources and the rotor plane reduces the effect of the steady pitching moment due to H-force.

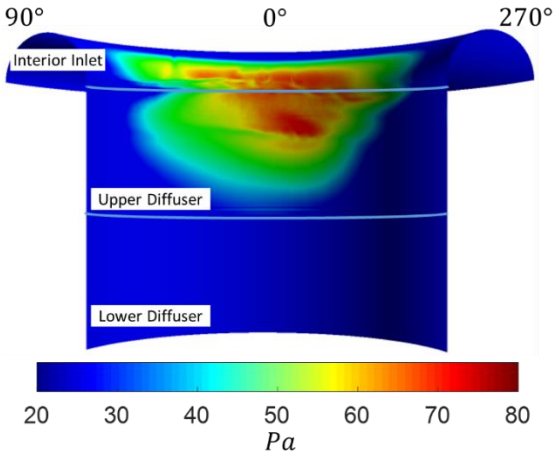

Figure 15: Pressure on duct surface looking at rear half of duct for 10 m/s forward flight case. Stagnation area observed near $\Psi = 0°$ is large source of drag

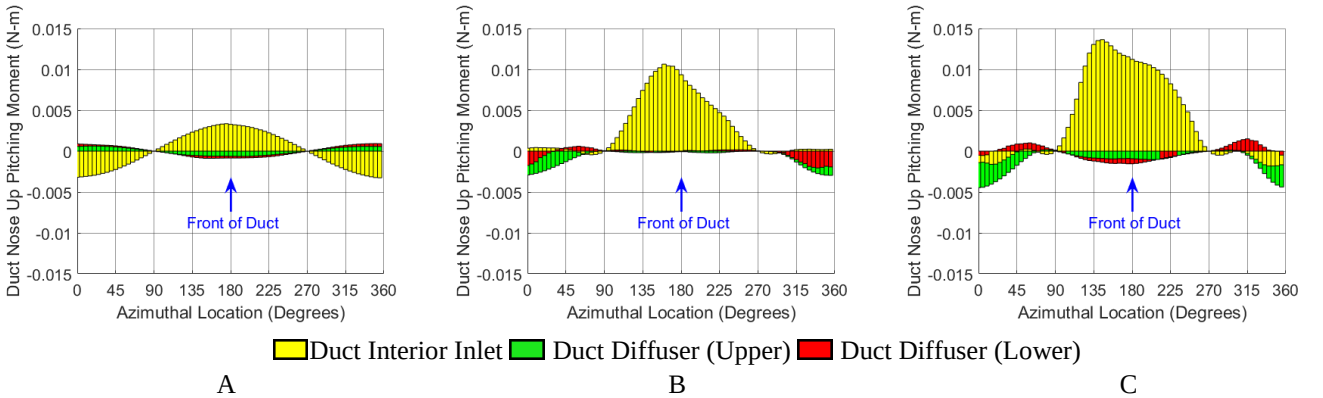

Figure 16: Azimuthal breakup of duct pitching moment in (A) hover, (B) 5 m/s, and (C) 10 m/s forward flight conditions time averaged over one rotor revolution

A much smaller side force and roll moment act on the duct and rotor hub. The azimuthal break up of these forces and moments is not presented. The small side force and rolling moment will be further discussed in the Ducted Rotor Performance section.

Ducted Rotor Performance

In addition to identifying the major sources for the generation of forces and moments (thrust, H-force, and pitching moment), this study also looked at these behaviors at the full aircraft level by integrating around the full azimuth and time averaging over a full revolution. The following results present the full aircraft behavior as forward flight speed varies from hover to 5 m/s, and 10 m/s. Figure 17 shows the change in thrust on the rotor and duct surfaces for the ducted fan.

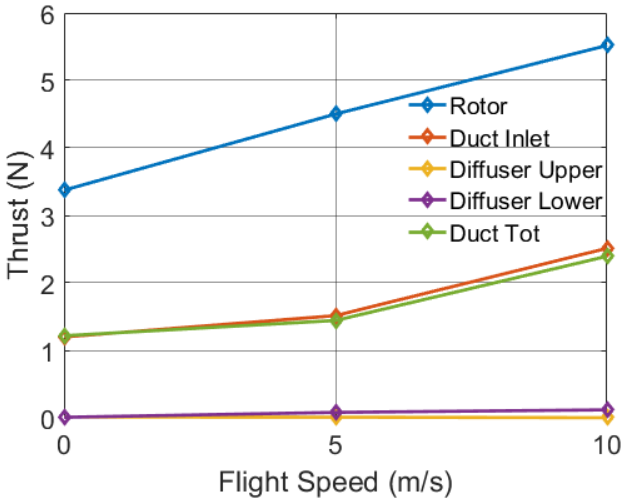

Figure 17: Thrust of rotor and interior duct surfaces versus translational flight speed

Over the analyzed range, rotor thrust increases linearly, seeing nearly a 60% increase in thrust at 10 m/s over the hover value. The rotor contributes 74%, 76% and 70% of the total thrust in hover, 5 m/s, and 10 m/s forward flight speeds respectively. The duct thrust is primarily generated on the duct inlet, as expected both diffuser sections are negligible in their contribution. The duct thrust increases over the analyzed speeds, and the duct contributes 26%, 24% and 30% of the total thrust in hover, 5 m/s, and 10 m/s forward flight speeds respectively.

Figure 18 shows the variation in rotor torque in the different flight conditions. The rotor in the ducted fan only sees modest increases in rotor torque (6%) over the analyzed flight conditions. The increase in dynamic pressure on the advancing blade increases the rotor drag near $\Psi = 90°$, but the upwash near the front of the disk decreases the sectional drag in this region near $\Psi = 180°$. Ultimately, the increase in dynamic pressure on the advancing blade outweighs the drag reduction in the upwash region and thus the net increase in rotor torque.

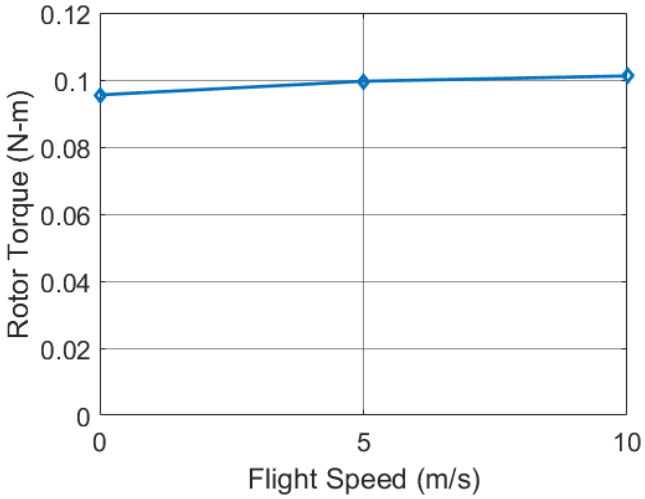

Figure 18: Rotor torque versus translational flight speed

Figure 19 shows the power loading (thrust per required power) of the rotor and combined rotor and duct. The duct adds "free" additional thrust since this simulation does not account for the additional power required to translate the ducted rotor system through the air at the specified flight speeds.

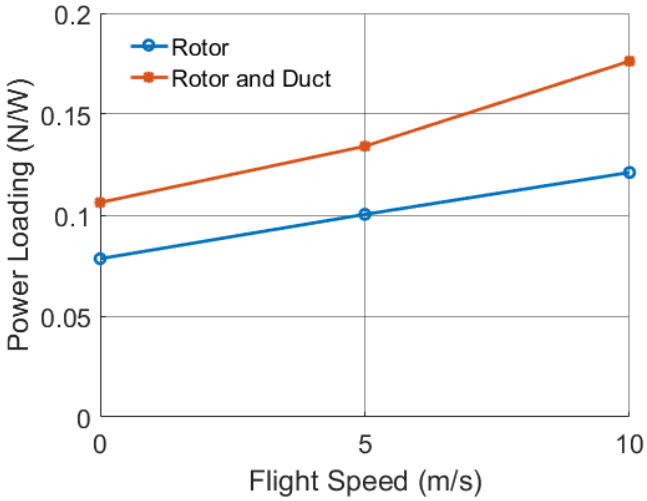

Figure 19: Power loading of the rotor and combined rotor and duct versus translational flight speed

The steady H-force, shown in Figure 20, comes primarily from the duct interior inlet and upper diffuser section. From the previous section looking at the azimuthal contributions to H-force (Figure 14), most of the drag contributed by the inlet comes from the suction on the interior inlet at the front of the duct. The H-force on the upper diffuser comes primarily from the ram drag as the freestream flow stagnates on the rear of the duct. Figure 20 shows the trends of the H-force at various flight speeds for the rotor and interior duct surfaces.

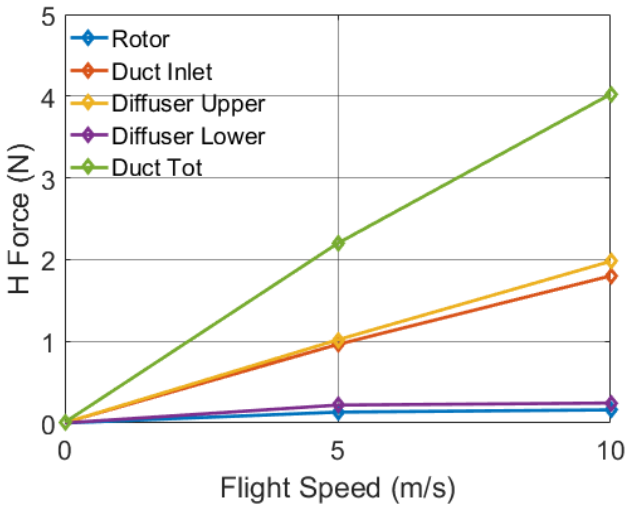

Figure 20: H-force of rotor and interior duct surfaces versus translational flight speed

Note that the rotor does not significantly contribute to the H-force and the rotor drag remains mostly constant with varying forward flight speed. Steady rotor H-force typically results from a large imbalance of drag on the rotor at $\Psi = 90°$ and $\Psi = 270°$, where the blades see the greatest difference in relative tangential velocity due to the freestream. At the analyzed flight conditions, the ducted rotor is operating at advance ratios of 0.075 and 0.15 respectively. While these are relatively low advance ratios, an open rotor at these advance ratios would still have a larger contribution to total H-force. Figure 21 shows the +X component of velocity (averaged over one revolution) in the rotor plane for 10 m/s forward flight conditions. The duct inlet shields the rotor from the true freestream velocity, and most of the rotor span encounters a +X component of velocity much less than the freestream value. The +X component of velocity at $0.75R$ span is 4.86 m/s. The result is the rotor operating at a lower effective advance ratio and thus less lateral imbalance of drag on the rotor and a lower H-force contribution from the rotor.

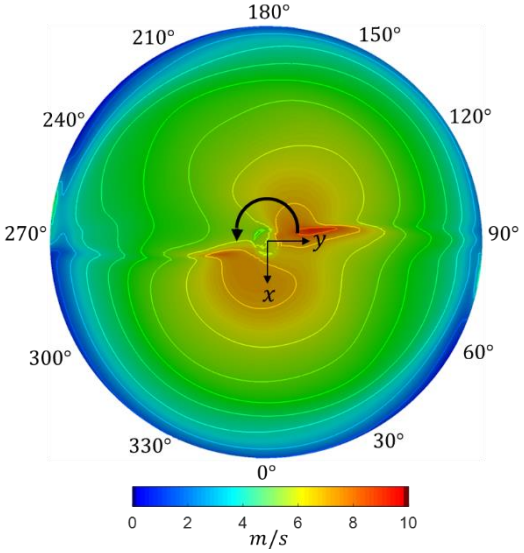

Figure 21: +X component of velocity (averaged over one revolution) in the rotor plane for 10 m/s forward flight condition

In addition to the small contribution from the rotor, the lower duct diffuser section has a small contribution to the total H-force. The H-force contributed by the duct interior inlet and upper diffuser section each contribute approximately 45% of the total duct H-force at the analyzed flight speeds. The contributions to total H-force are decomposed by component in Table 3.

Table 3: Component decomposition and their contributions to H-force in forward flight conditions

Component	Contribution to Total H-force at 5 m/s	Contribution to Total H-force at 10 m/s
Rotor	6%	4%
Duct Interior Inlet*	44%	46%
Duct Diffuser (Upper)**	44%	46%
Duct Diffuser (Lower)	6%	4%
Duct Total	94%	96%

* Predominantly from front
** Predominantly from rear

Figure 22 shows the variation in pitching moment versus flight speed. The thrust on the front of the duct inlet (Figure 11) and the upwash region increasing the rotor blade's effective angle of attack at the front of the disk (Figure 7 and Figure 8) explains the net nose up pitching moment. Both these conditions grow with flight speed, increasing the nose up pitching moment on the duct inlet and rotor. The rotor contributes 24% and 44% of the total nose up pitching moment at 5 and 10 m/s respectively. The upper and lower diffuser sections produces a nose down pitching moment due to the ram drag at the rear of the duct, but this only partially negates the nose up pitching moment from the inlet.

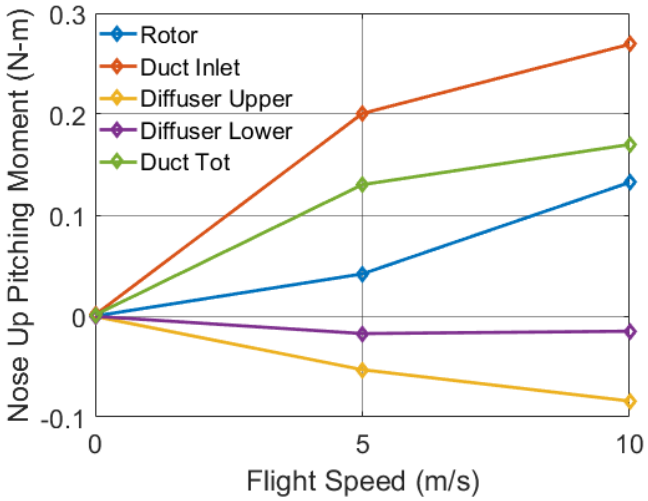

Figure 22: Pitching moment of rotor and interior duct surfaces versus translational flight speed

Finally, the steady side force and accompanying roll moment from this study were observed to be small compared to the dominant forces and moments of the system (thrust, H-force, and pitching moment); the calculated values are at the limit of the accuracy level of this study. As the steady side force and

rolling moment were small, only the values for the 10 m/s forward flight case are reported in Table 4 below.

Table 4: Steady side force and roll moment of the rotor and interior duct surfaces for the 10 m/s case

	Side Force East (N)	Roll Mom. Left (N-m)
Rotor	0.0005	0.02777
Interior Inlet	-0.1012	0.03594
Upper Diffuser	0.1023	0.00087
Lower Diffuser	-0.0610	-0.01009
Duct Total	-0.0599	0.02672

Vibratory Loads

In addition to the steady vehicle loads, the vibratory loads associated with the blade passage frequency were also analyzed as part of this study. Both the rotor and the duct are sources of vertical and in-plane vibrations. The rotor vertical and in-plane vibrations come from azimuthal variation in the blade root vertical shear S_z and chordwise shear S_x. Figure 23 shows the blade root vertical shear at 10 m/s forward speed. The $S_{z_{2p}}$ of each blade contributes to the rotor vertical vibration while the $S_{z_{1p}}$ vibrations are canceled at the hub for a two-bladed rotor.

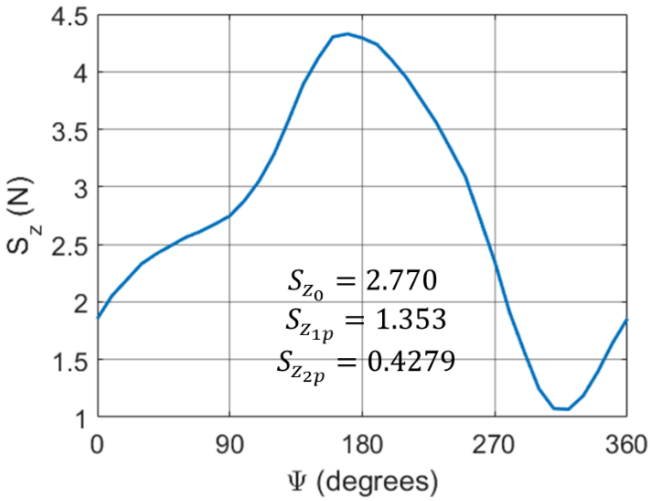

Figure 23: Blade root vertical shear over one revolution at 10 m/s forward speed

Figure 24 shows the blade chordwise (drag) shear loads over one revolution. Note that the magnitude of $S_{x_{1p}}$ vibration, is the source of the rotor hub in-plane vibrations.

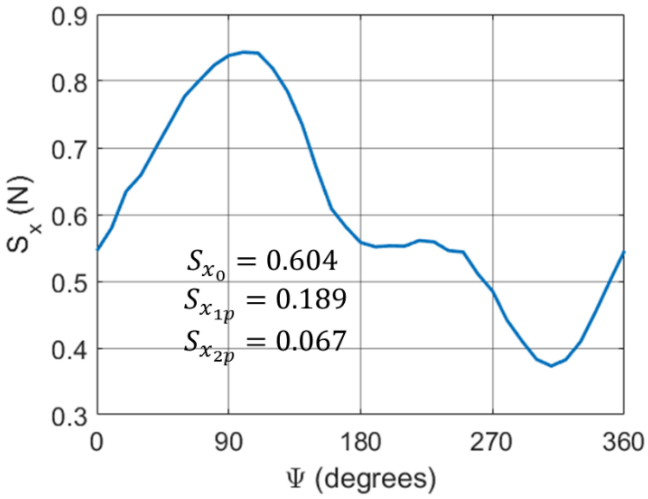

Figure 24: Blade root chordwise shear over one revolution at 10 m/s forward speed

The duct is also a significant contributor to the in-plane vibrations. Due to the very small clearance between the rotor tip and duct wall the high pressure on the lower surface of the blade and the low pressure on the upper surface at the tip exert local forces on the duct. Figure 25 shows the pressure on the surface of the duct immediately adjacent to the blade tip at various azimuthal locations.

Note in Figure 25 the suction on the duct above the blade tip and the higher pressure on the duct wall below the rotor tip at any azimuthal location do not cancel, resulting in a net force that contributes to in-plane vibratory loads. Additionally, the magnitude of the in-plane H-forces generated at the front of the disk ($\Psi = 135°, 180°,$ and $225°$ on Figure 25) are much higher than those at the rear (due to the higher lift generated by the rotor blades at the front), creating further azimuthal variation in in-plane forces on the duct. The suction above the blade and high pressure below the blade also induces a net moment about the rotor plane.

Figure 26 shows how the presence of the blades affects the azimuthal distribution of duct pitching moment for the 10 m/s forward flight condition. The black lines in the figure represent the quarter chord line of the blades.

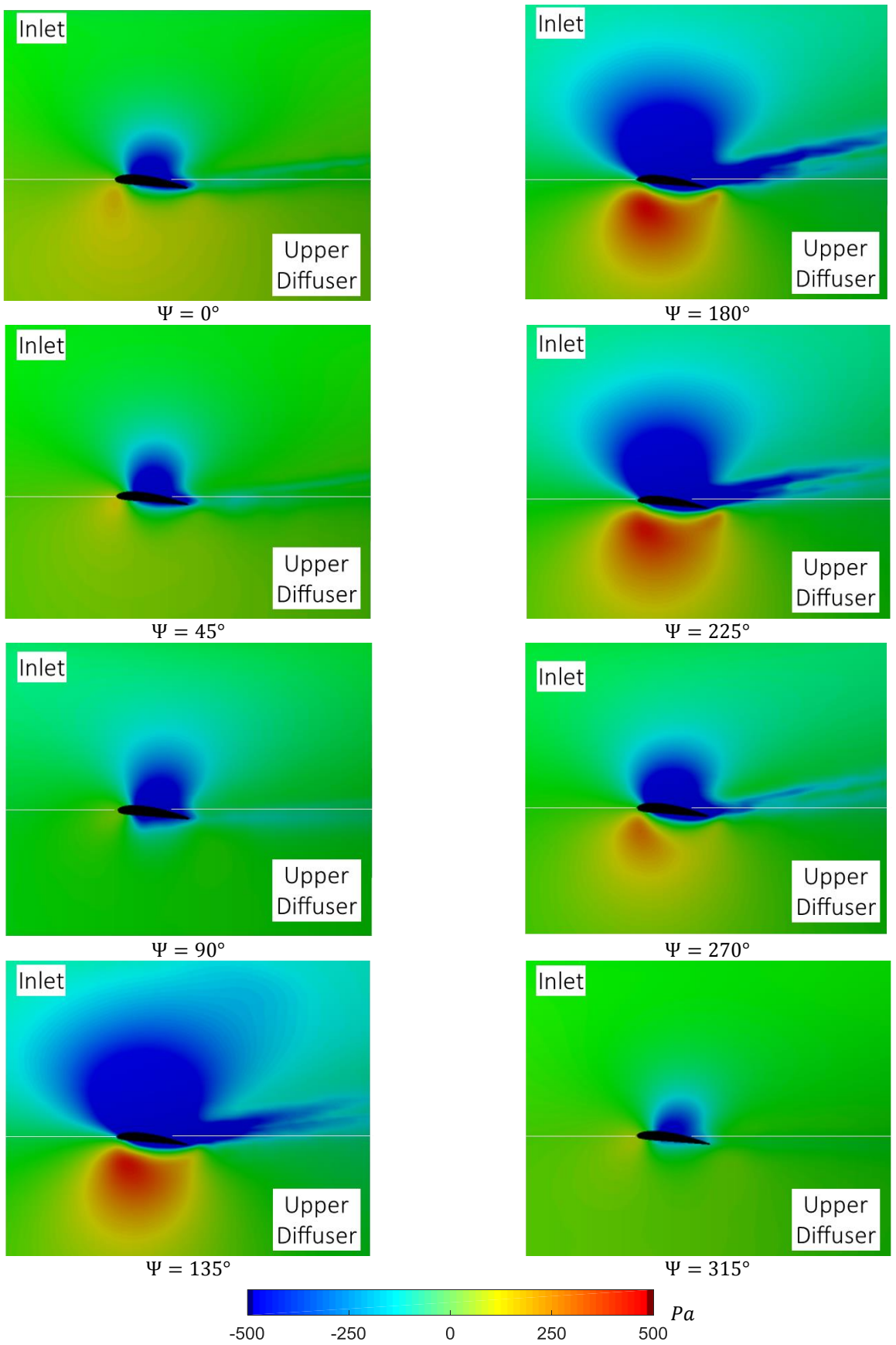

Figure 25: Pressure contours on duct inlet and upper diffuser adjacent to rotor tip at various azimuth positions

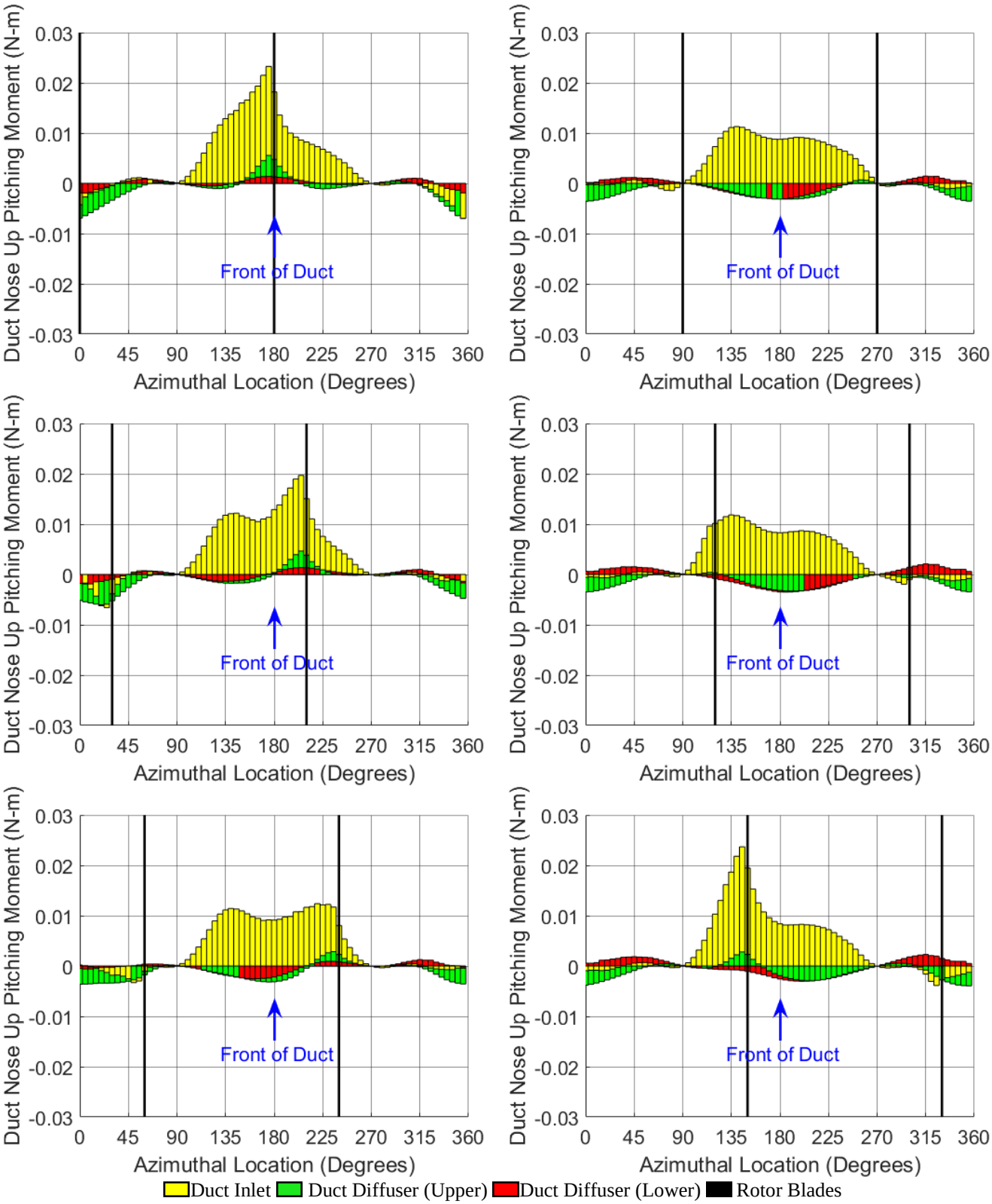

Figure 26: Azimuthal breakup of duct pitching moment with presence of blades, translating at 10 m/s

Comparing the time dependent duct pitching moment (Figure 26) to the time averaged steady duct pitching moment (Figure 16 C), the local pressure at the blade tips either adds to the steady pitching moment, as is the case on the duct inlet near $\Psi = 180°$, or opposes the steady pitching moment, as the case on the upper diffuser. Note how when the blade is at $\Psi = 180°$ in Figure 26, the pitching moment on the upper diffuser section at the front of the disk is positive and nose up. In Figure 16 C, the steady pitching moment on the diffuser sections at $\Psi = 180°$ is nose down. This high pressure from the bottom surface of the rotor blade produces a nose up pitching moment relative to the rotor hub. At the same azimuthal location the suction from the upper surface of the blade acts on the duct inlet. This produces additional lift on the inlet and nose up pitching moment in the presence of the blade. The pitching moment in Figure 26 is an illustrative example of the position of the rotor blades affecting the local moments on the duct, but the same phenomena is present in all forces and moments acting on the duct and is the reason for the duct vibratory loads.

Figure 27 and Figure 28 show the instantaneous H-force and side force for the duct components at the 10 m/s forward flight case. Positive F_x represents force in the drag direction and positive F_y is a side force out the starboard side of the rotor. These figures show the instantaneous vibratory loads (the steady loads have been removed) when the blades begin at 0° and 180°. The F_x and F_y vibratory loads share similar magnitudes on the corresponding components. The inlet and upper diffuser are 180° out of phase, this comes from a low pressure suction acting on the inlet while a high pressure acts on the upper diffuser. The magnitude of the in-plane vibratory loads on the inlet is smaller than on the upper diffuser. Figure 25 shows that the suction region above the blade is stronger and affects a larger area than the high pressure region below the blade. However, the curvature of the inlet breaks the force exerted by this pressure into an in-plane component (shown in Figure 27 and Figure 28) and a vertical component. The upper and lower diffuser vibratory loads are in phase. The high pressure causes an outward force on the upper diffuser and this effect carries to the lower diffuser. The magnitude of the force on the lower diffuser is reduced because it is further from the source of the high pressure. The upper diffuser is the largest contributor to the in-plane vibratory forces.

Figure 29 and Figure 30 show the instantaneous pitching and rolling moment vibrations taken about the rotor hub, for the duct components at the 10 m/s forward flight case. Positive M_y represents a nose up pitching moment and positive M_x is a roll left moment. In Figure 29 and Figure 30 the steady moments have been removed and the blades begin at 0° and 180°. The pitching moment vibrations are slightly smaller in magnitude than the rolling moment induced vibrations. From the moment analysis all components of the duct are in phase as the suction acts above the rotor plane while the pressure acts below the rotor plane. All three duct interior components induce vibrations of similar magnitudes. While the lower diffuser sees smaller in-plane vibratory loads than the upper diffuser, it has a longer lever arm to the rotor hub, increasing its effect on moment induced vibrations. The duct inlet is not largely separated from the rotor plane in the vertical direction, however, the curvature of the inlet increases its contribution to moment vibrations. When the suction from the top of the blade acts on the inlet the resultant force is normal to the surface, one component in the radial in-plane direction and the other component in the vertical direction. This vertical component of the force has the radius of the duct acting as a lever arm and this accounts for the pitching and rolling moment vibrations induced by the duct inlet.

The vibrations were examined at flight speeds of 5 and 10 m/s. The contribution of each duct surface was analyzed separately and the full duct is the summation of all the interior surfaces. Lastly, the vibratory signals of the duct and rotor were combined to assess the vibratory loads at the full aircraft level. Figure 31 shows the magnitude of the 2/rev vertical vibrations at the analyzed flight speeds.

The rotor is the largest contributor to total aircraft vibrations (93% at 10 m/s). The duct inlet is the only duct surface that significantly contributes to the vertical vibrations. The vertical vibratory loads from the rotor are nearly 15% of the steady rotor thrust at 10 m/s.

While the side force and rolling moment were negligible in their steady load contributions, the vibratory loads are substantial. Figure 32 and Figure 33 show that the in-plane vibratory loads in the longitudinal and lateral directions are of similar magnitude at the same flight speeds.

For the in-plane vibratory loads the upper diffuser is the largest contributor and the entire duct contributes approximately 65% and 75% of the total longitudinal and lateral vibrations respectively. For the full ducted fan, the amplitude of the longitudinal in-plane vibration is 15.3% of the steady total H-force load.

Similarly to the in-plane vibrations, the vibrations induced by the pitching moment (Figure 34) and rolling moment (Figure 35) are comparable in magnitude when analyzed at the same flight speeds.

Figure 34 and Figure 35 show the rotor is the largest contributor to the moment induced vibrations (67% of the pitching and 65% of the rolling). The magnitude of the full ducted fan pitching moment vibrations are over 61.5% of the steady total pitching moment at 10 m/s.

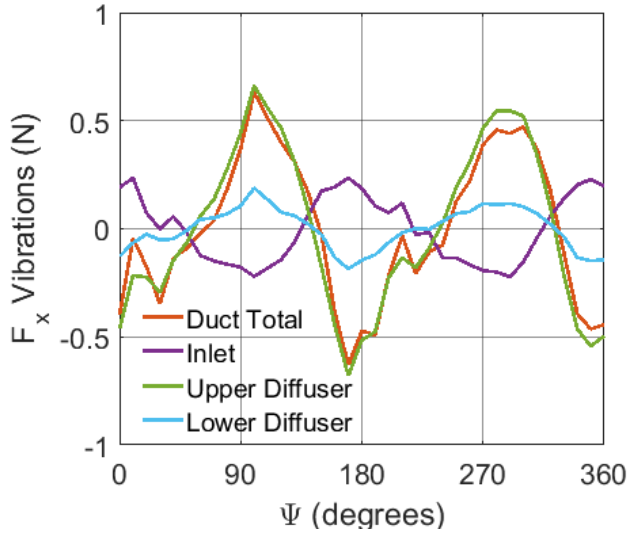

Figure 27: Instantaneous H-force on duct components for 10 m/s case when the advancing blades starts at 0° and moves around the azimuth

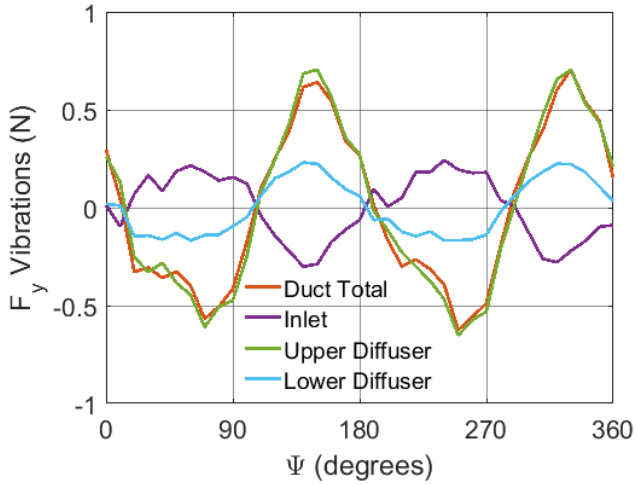

Figure 28: Instantaneous side force on duct components for 10 m/s case when the advancing blades starts at 0° and moves around the azimuth

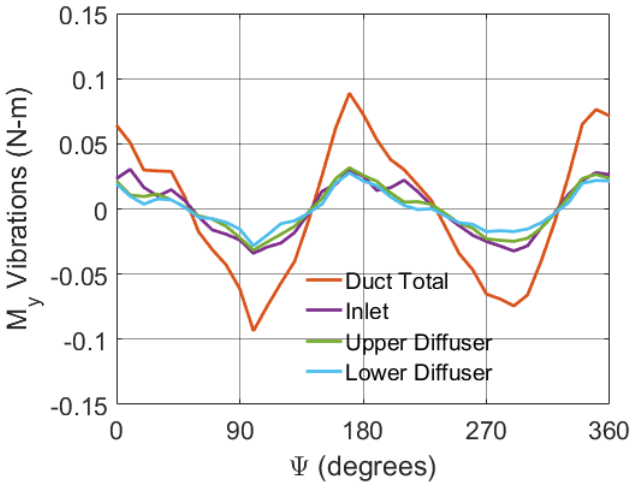

Figure 29: Instantaneous pitching moment on duct components for 10 m/s case when the advancing blades starts at 0° and moves around the azimuth

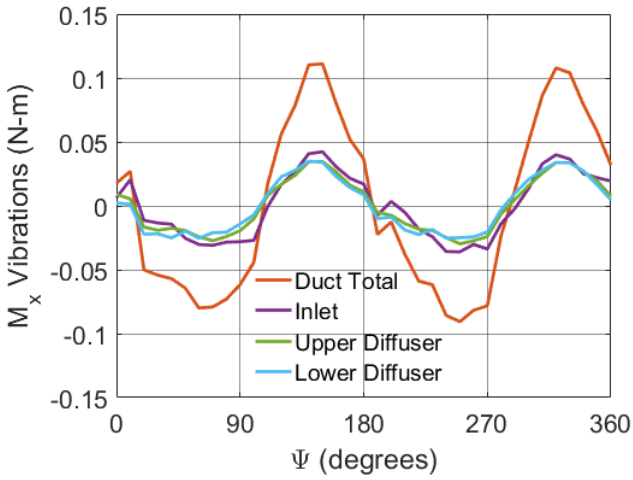

Figure 30: Instantaneous rolling moment on duct components for 10 m/s case when the advancing blades starts at 0° and moves around the azimuth

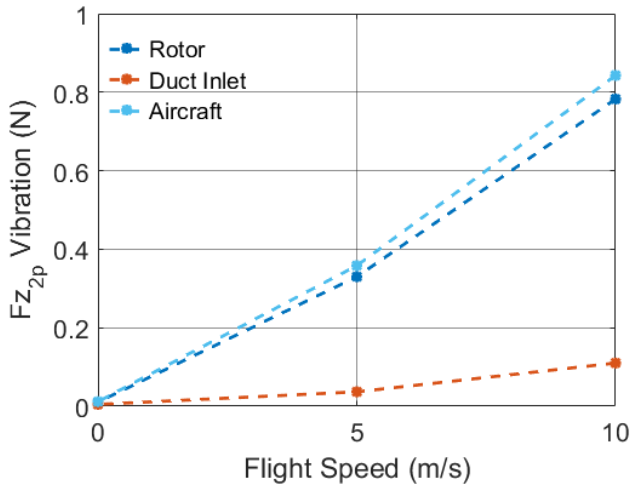

Figure 31: Rotor and duct contributions to vertical vibrations in hover and forward flight conditions

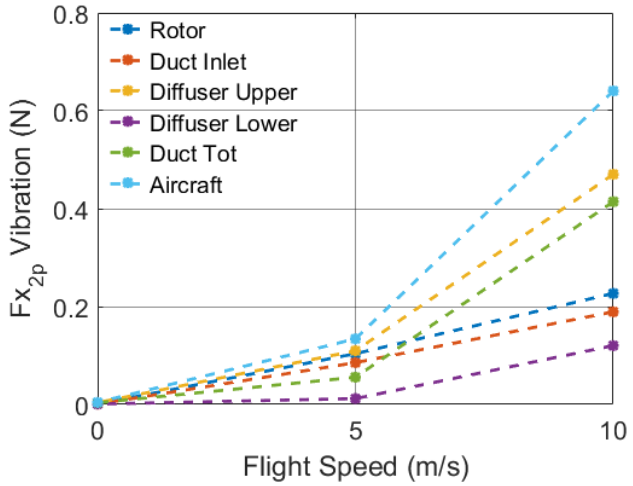

Figure 32: Rotor and duct contributions to longitudinal vibrations in hover and forward flight conditions

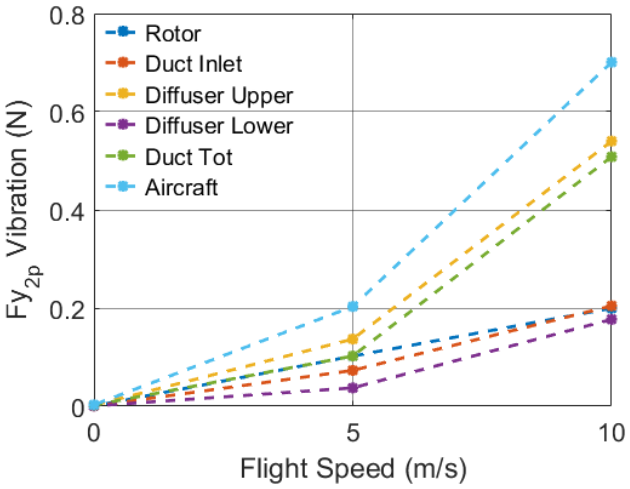

Figure 33: Rotor and duct contributions to lateral vibrations in hover and forward flight conditions

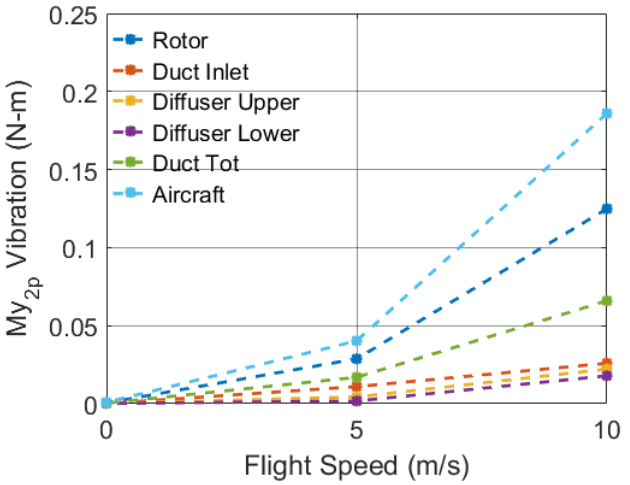

Figure 34: Rotor and duct contributions to pitching moment vibrations in hover and forward flight conditions

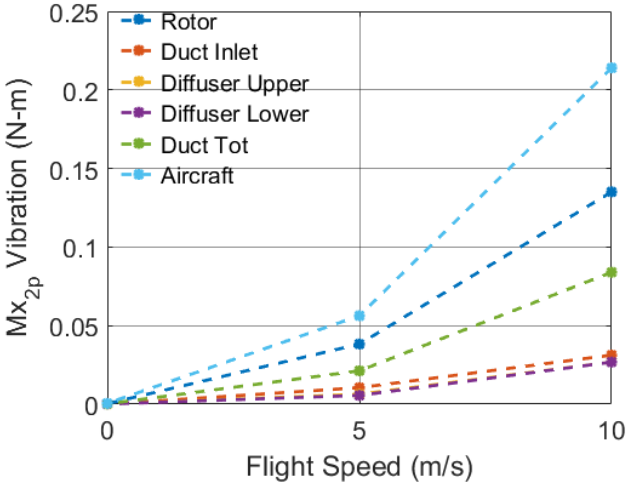

Figure 35: Rotor and duct contributions to rolling moment vibrations in hover and forward flight conditions

CONCLUSIONS

Using a three dimensional RANS CFD model, a ducted rotor was simulated with a sliding mesh to analyze its behavior in hover, 5 m/s, and 10 m/s forward flight conditions given zero nose down attitude. This study examined the rotor and interior sections of the duct and determined the influence of each component on the performance. A detailed examination of the flow physics was used to understand the ducted rotor behavior. The dominant steady forces and moments were analyzed as well as the vibratory loads on the ducted rotor system. The complex flow phenomena and rotor-duct interactions are explained as they pertain to the performance.

When the ducted fan is in edgewise flight conditions the freestream flow separates off the front of the duct inlet. In this region of separation, the flow recirculates, resulting in an upwash at the front of the disk. The increased effective angle of attack in this region shifts the thrust produced by the rotor to the front of the disk. This differs significantly from the behavior of a fixed pitch open rotor where the greatest thrust variation would be lateral due to difference in advancing and retreating side dynamic pressure. As the blade interacts with the separation region the relative upwash seen by the rotor shifts inboard. In addition, the rotor swirl biases the upwash region slightly to the retreating side.

Unlike the maximum thrust which is seen at the front of the disk, the maximum rotor drag is observed on the advancing side. At the front of the disk although the lift is the highest the upwash reduces the induced drag, thereby limiting the total drag. The maximum drag on the advancing side is observed in the mid-span region rather than the outboard sections due to the high twist and taper ratio of the blade.

In forward flight the duct produces significant thrust over the front section of the inlet. Rotor swirl velocity biases the separation region on the duct inlet to the retreating side which causes a slight lateral asymmetry in inlet dominated thrust production. The duct accounts for up to 30% of the total thrust at 10 m/s.

The interior of the duct is the dominant source of drag contributing up to 96% of the total H-force at 10 m/s. The suction on the front of the duct inlet and ram pressure on the rear of the upper diffuser contribute in equal measure.

The duct contributes up to 56% of the total nose up pitching moment at 10 m/s. The lift on the front of the inlet is the primary source of the duct nose up pitching moment but this is partially negated by the ram pressure on the rear of the diffuser. The rotor also significantly contributes to the nose up pitching moment due to the upwash biasing thrust to the front of the disk.

The rotor is the dominant source of the vertical 2/rev vibratory force and is responsible for 93% of the total vertical vibration at 10 m/s. Due to the small tip clearance, the region of the duct right below the blade tip experiences a high pressure while the

region just above sees a suction. As a result of the imbalance of these pressure regions, as well as azimuthal variation, the duct experiences 2/rev in-plane vibratory forces. The duct contributes 65% of the longitudinal vibratory force and 75% of the lateral vibratory force at 10 m/s.

The rotor is the primary contributor to the 2/rev vibratory moments generating 67% of the total pitching moment and 63% of the total rolling moment at 10 m/s. The significant 1/rev variation in rotor thrust around the azimuth is the cause of these moments.

In summary, both the rotor and duct produce additional thrust when going from hover to edgewise flight conditions. The interior of the duct is a significant source of drag due to suction on the front of the duct and ram pressure on the rear. Both the duct and rotor contribute to a strong nose up pitching moment. Finally, the rotor is a dominant producer of vertical vibratory forces and vibratory pitching and rolling moments while the duct is primarily responsible for the in-plane vibratory forces.

Author contact: Matthew Misiorowski misiom@rpi.edu, Farhan Gandhi fgandhi@rpi.edu, Assad Oberai oberaa@rpi.edu

ACKNOWLEDGMENTS

The authors would like to thank Rensselaer Polytechnic Institute and the Center for Computational Innovations. The findings from this study are only possible thanks to the availability of their computing resources and dedicated staff that maintain the network and hardware.

REFERENCES

1. Ziegenbein, P., "PhantomSwift Quad-Ducted Rotor Aircraft Configuration Development," American Helicopter Society 72nd Annual Forum, West Palm Beach, FL, May 2016.
2. Tatro, J., Yoeli, R., and Samples, D., "X-Hawk: Transformational Mobility for the Urban Warfighter," American Helicopter Society 62nd Annual Forum, Phoenix, AZ, May 2006.
3. Hirschberg, M., *A Small Lighting Strike*, Vertiflite July-Aug 2016, pp. 10-11.
4. Kruger, W., "On Wind Tunnel Tests and Computations Concerning the Problem of Shrouded Propellers," NACA TN 1202, 1949.
5. Leishman, J. G., *Principles of Helicopter Aerodynamics*, 2nd Edition, Cambridge University Press, New York, NY, 2006, pp. 321-324.
6. Pereira, J. and Chopra, I., "Surface Pressure Measurements on an MAV-Scale Shrouded Rotor in Hover," American Helicopter Society 62nd Annual Forum, Phoenix, AZ, May 2006.
7. Pereira, J. and Chopra, I., "Performance and Surface Pressure Measurements on a MAV-Scale Shrouded Rotor in Translational Flight," American Helicopter Society 63rd Annual Forum, Virginia Beach, VA, May 2007.
8. Hook, R., Myers, L., and McLaughlin, D., "Investigation on Flow Physics of Edgewise Ducted rotor Air Vehicles," American Helicopter Society 67th Annual Forum, Virginia Beach, VA, May 2011.
9. Hook, R., Myers, L., and McLaughlin, D., "A Study of Leading Edge Shapes for the Front Duct of a Dual Ducted Rotor Vehicle," American Helicopter Society 67th Annual Forum, Virginia Beach, VA, May 2011.
10. Martin, P., and Tung, C., "Performance and Flowfield Measurements on a 10-inch Ducted Rotor VTOL UAV," American Helicopter Society 60th Annual Forum, Baltimore, MD, June 2004.
11. Martin, P., and Boxwell, D. A., "Design, Analysis and Experiments on a 10-Inch Ducted Rotor VTOL UAV," AHS International Specialists Meeting on Unmanned Rotorcraft: Design, Control and Testing, Chandler, AZ, Jan. 2005.
12. Akturk, A., and Camci, C., "Experimental and Computational Assessment of a Ducted-Fan Rotor Flow Model" *Journal of Aircraft*, Vol. 49, (3), May – June 2012, pp. 885-897.
13. Akturk, A., and Camci, C., "Influence of Tip Clearance and Inlet Flow Distortion on Ducted rotor Performance in VTOL UAVs," American Helicopter Society 66th Annual Forum, Phoenix, AZ, May 2010.
14. Akturk, A., and Camci, C., "Lip separation and Inlet Flow Distortion Control in Ducted Fans Used in VTOL Systems," ASME turbo Expo, Dusseldorf, Germany, June 2014.
15. Singh, R., and Dinavahi, S., "Shape Optimization of a Ducted Rotor System for Aerodynamic Performance," 49th AIAA Aerospace Sciences Meeting, Orlando, FL, Jan. 2011.
16. Jimenez, B., and Singh, R., "Effect of Duct-Rotor Aerodynamic Interactions on Blade Design for Hover and Axial Flight,"53rd AIAA Aerospace Sciences Meeting, AIAA SciTech, Kissimmee, FL, Jan. 2015.
17. Corson, D., Rajeev, J., and Farzin, S,. "Industrial application of RANS modelling: capabilities and needs." *International journal of Computational Fluid dynamics* 23.4 (2009): 337-347.
18. Simmetrix "MeshSim –Automatic Mesh Generation." http://www.simmetrix.com/products/SimulationModelingSuite/MeshSim/MeshSim.html, 1997.